Orbital-selective metallicity in the valence-bond liquid phase of Li_2RuO_3

Patrick McArdle,[1] Fei-Ting Huang,[2] Junjie Yang,[3] Ming-Wen Chu,[4] Sang-Wook Cheong,[2] and M. Mumtaz Qazilbash[1,*]

[1]*Department of Physics, College of William & Mary, Williamsburg, Virginia 23187-8795, USA*

[2]*Rutgers Center for Emergent Materials and Department of Physics & Astronomy, Rutgers University, Piscataway, New Jersey 08854, USA*

[3]*Department of Physics, New Jersey Institute of Technology, Newark, New Jersey 07102, USA*

[4]*Center for Condensed Matter Sciences and Center of Atomic Initiative for New Materials, National Taiwan University, 106 Taipei, Taiwan*

(Received 3 January 2022; revised 15 April 2022; accepted 27 May 2022; published 29 June 2022)

Li_2RuO_3 (LRO) forms a valence bond crystal at room temperature. It undergoes a high temperature phase transition that involves structural, magnetic, and electronic changes leading to an exotic valence bond liquid state. The orbital degrees of freedom are thought to be fundamental to the evolution of LRO properties across the phase transition. We report temperature dependent broadband (100–26 000 cm^{-1}) reflectance measurements on single crystals of LRO to elucidate structural and transport properties. Specifically, the phonon and electronic properties of LRO were investigated through the phase transition. We report that above the transition temperature ($T_c \approx 500$ K), the optical band gap closes for electrons in the d_{xz}/d_{yz} orbitals, but the d_{xy} electrons remain gapped. This behavior at high temperature can be associated with an orbital selective metallic state which to our knowledge has not been previously reported in LRO.

DOI: 10.1103/PhysRevB.105.245148

I. INTRODUCTION

Competitive interactions on the honeycomb lattice among the fundamental lattice and electronic degrees of freedom (phonons, charge, spin, orbital) can lead to realization of novel physical properties such as potential quantum spin liquid states [1,2], interesting topological properties [3], massless Dirac fermions seen in graphene [4], or quasimolecular orbital formation [5]. For some 4*d* and 5*d* transition metal (TM) compounds, the orbital degrees of freedom (DOF) can play a dominant role in the formation of the ground state configuration [6]. Competition between relative strengths of the electron-electron interaction, Hund's coupling, and orbital overlap involving neighboring sites can lead to electrons from different orbitals to decouple from each other. This orbital selectivity has recently been connected to iron based high-temperature superconductors and heavy fermion systems [7–9], thus emerging as a key ingredient to novel phenomena. On the honeycomb lattice, this behavior is widely expected due to the edge or face sharing nature of neighboring sites, such as in Li_2RuO_3 (LRO).

LRO forms a lattice of strong singlet dimer bonds or valence bond crystal (VBC) at ambient temperature and pressure [10]. The Ru-Ru dimers form in the plane of the honeycomb lattice of Ru ions. The VBC state can be realized in other honeycomb materials such as $\alpha-RuCl_3$ but usually requires external pressure [11–13]. The Ru valence electrons in LRO that do not participate in the dimerization form weak molecular bonds and can be largely treated as site centered atomic orbitals [14]. This is evidenced by a reduced magnetic susceptibility at low temperatures, which is expected because of the lack of spin contribution from singlet dimer formation [15]. Furthermore, *dc* transport measurements do not display activation behavior in the insulating VBC phase, but instead show variable range hopping [10,16,17]. In the insulating VBC phase, LRO is expected to have a very small band gap due to weakly bound out of plane molecular bonds [18]. Interestingly, heat capacity measurements on both stoichiometric and disordered LRO, find a linear contribution at low temperatures [16]. This seems indicative of some electronic behavior below the quenching temperature of the phonons. However, the origin of this property has also been attributed to potential low energy magnetic excitations (singlet-triplet excitations) [16].

The long-range ordering of dimers in the VBC state survives up to $T_c \approx 500$ K. Above this temperature, it has been suggested that LRO melts into a valence bond liquid (VBL) following a structural transition [15]. In the proposed VBL state, the dimer patterns survive only locally and flow throughout the system via random thermal fluctuations. This same study [15] found experimentally that dimers survive up to ≈920 K, and they estimate that dimers may survive all the way up to ≈1550 K. The temperature estimate for dimer disassociation (≈1550 K) is based on DFT analysis [15] and is higher than the decomposition temperature of LRO (≈1300 K) ref [19], indicating the strong energy preference for dimerization. Accompanying the structural transition is an abrupt rise in magnetic susceptibility and decrease in resistivity [10]. These changes in the physical properties have been attributed to the delocalization of weakly bonded electrons in the out-of-plane orbitals [20]. This implies an orbital selectivity between the delocalized and valence-bonded electrons and would also explain the nearly free spin-½ magnetic contribution to the susceptibility at high temperatures [21] The drop in resistivity was initially described as a transition to a correlated metallic phase [18]. Recent resistivity measurements and density functional calculations (DFT) in the high temperature phase exhibit clear activation energy which has been ascribed

*Corresponding author: mmqazilbash@wm.edu

to the existence of a band gap [17]. Since DFT is a $T = 0$ technique, it is difficult to assess the applicability of these results to high temperature properties. Due to the observed orbital selectivity, one could also expect a potential hybrid phase with correlated metallic properties due to the delocalized electrons and an insulating (pseudo)gap due to thermally activated dimers. Although to date, direct measurements of the band gap and energy dependent conductivity to characterize such a hybrid phase in LRO have not been done.

In this paper, we present broadband temperature dependent reflectance measurements on single crystals of LRO. Optical spectra enable us to characterize the phonon and electronic properties of LRO from the VBC through VBL phases. This approach allows us to directly observe the band gap and electronic transitions in the VBC phase and to investigate the high temperature carrier dynamics in the VBL phase. Additionally, we corroborate the expected high-temperature structural transition through the study of the infrared phonon spectra.

II. EXPERIMENTAL METHODS

Single crystals of LRO were grown from LiCl flux with proper molar ratio of Li_2CO_3 and RuO_2 and then were slow cooled in the temperature range between 1020 °C and 850 °C. LRO single crystals form a triangular prism with about half millimeter length of the edge [Fig. 1(a)]. The lattice structure of our single crystals was determined using transmission electron microscope (TEM). Specimens for TEM studies were prepared by scotch-tape cleavage, followed by Ar-ion milling, and studied using a JEOL-2010F TEM at Rutgers University. The as-grown surface is perpendicular to [101] of monoclinic $P2_1/m$ structure [10]. High-angle annular dark-field (HAADF) scanning TEM imaging with atomic-column resolution was carried out using a JEOL-2100F microscope equipped with a spherical aberration Cs-corrector at National Taiwan University in Taiwan. The distinct feature of Ru-Ru dimer as shown in HAADF-STEM image of Fig. 1(c) and the appearance of $(h0l)$, $h =$ odd and $(hkl)h + k =$ odd peaks along [101] (red arrows in Fig. 1(d)) confirm the $P2_1/m$ structure of our single crystals at room temperature. This is important since single crystal LRO can form in the $P2_1/m$ or $C2/m$ structure at room temperature [22]. Note that those Bragg peaks [marked by red arrows in Fig. 1(d)] in the selected area electron diffraction pattern are forbidden in the higher symmetry ($C2/m$) structure. The crystal structure ($P2_1/m$) of LRO in the ab plane at room temperature is shown in Fig. 1(b). Crystallographic x-ray diffraction (XRD) data [18] were used to produce the crystal structure displayed in Fig. 1(b) with the software package VESTA [23].

Infrared and optical reflectance is an ideal measurement probe to study both the lattice and electronic degrees of freedom simultaneously. The reflectance measurements were performed at William & Mary. Due to the small size of the crystals [Fig. 1(a)], it was necessary to perform the reflectance measurements with a microscope that allowed us to focus the incident light to a spot smaller than the crystal size. The Spectra-Tech IR-Plan microscope was coupled to a Bruker Vertex 80v vacuum spectrometer. Light from the spectrometer was directed toward the microscope through an optically transparent window in the spectrometer's light output port. A KBr window with antimoisture coating was used for mid-infrared through visible spectral range, and a polypropylene window was used in the far-infrared spectral range. To remove atmospheric absorbances from the far- and mid-infrared spectra, the spectrometer was held in vacuum and the microscope was enclosed in a dry air purge free of CO_2 and H_2O. Schematic of the microscope aperture, Schwarzschild objective (NA = 0.58), and sample/reference stage is displayed in Fig. 2(a). The sample stage and reference stage were aligned to maximize the reflectance through the aperture from the surface of the LRO crystal and the surface of the reference material. The dimensions of the upper aperture, and magnification of the objective sets the approximate spot size at the sample. The magnification of our objective was fixed at ×15, and the aperture sizes used for each spectral range are listed in Table I. Reflectance spectra were obtained between 100 and 26 000 cm^{-1} in 100 K temperature intervals, from 300 to 600 K. Data were obtained at 100 K intervals to minimize the time spent at elevated temperatures which ensured the intrinsic properties of our crystals were being captured. We were unable to obtain reliable reflectance values into the ultraviolet spectral range (frequency > 26 000 cm^{-1}) due to low signal-to-noise. Table I also contains the frequency range,

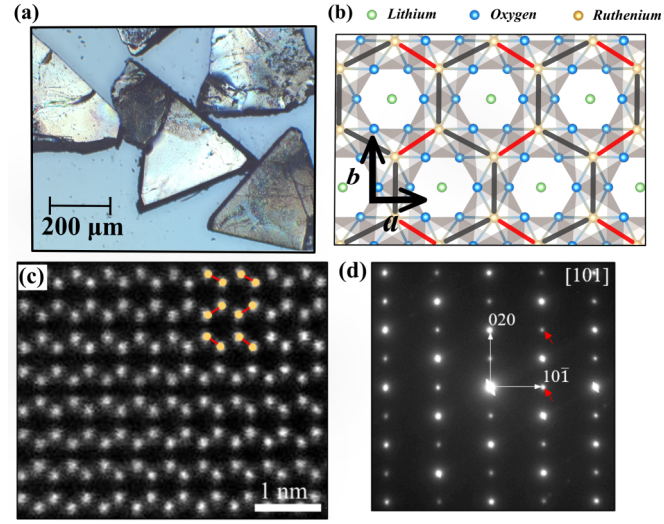

FIG. 1. (a) Optical microscope image of our Li_2RuO_3 (LRO) single crystals used for reflectance measurements; [101] is perpendicular to the flat surfaces shown. (b) View of ab plane for the room temperature monoclinic ($P2_1/m$ space group) phase with axes orientation shown by the arrows. Red lines represent dimer bonds and black lines are nondimerized bonds between Ru-Ru ions. Edge sharing RuO_6 octahedra are contained in the grey shaded areas. Above $T_c \approx 500$ K, the average structure is expected to conform to a monoclinic (C2/m space group, nondimerized structure). (c) The room temperature atomic-resolved HAADF-STEM image of Li_2RuO_3 crystal along the [101] zone axis. Overlaid color-coded Ru-Ru dimers are defined by the shortest Ru-Ru atomic columns. (d) The selected area electron diffraction (SAED) pattern of Li_2RuO_3 crystal along [101]. Red arrows indicate (h0l), h = odd and (hkl) h + k = odd peaks, which are not allowed in the high symmetry C2/m and confirm the $P2_1/m$ structure of our crystals.

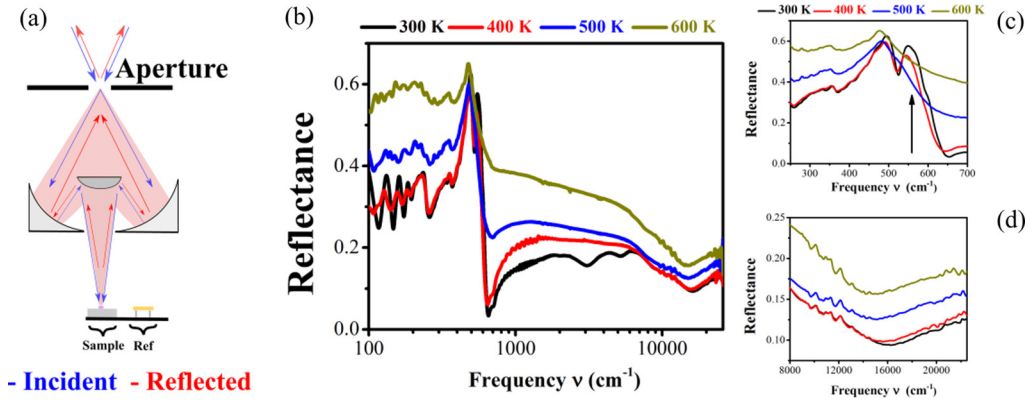

FIG. 2. (a) Focusing optics employed in experiment. Blue arrows represent the incident beam from the FTIR interferometer. The incident beam is focused on either sample or reference at near-normal incidence using a Schwarzschild type objective. The reflected beam is collected by the same objective and sent to the detector. (b) Temperature dependent absolute reflectance on single crystals of LRO. (c) Shows zoomed in perspective of reflectance in the spectral range 250–700 cm^{-1}. Black arrow indicates the large Ru-O phonon feature that is strongly modified by the structural transition at $T \approx 500$ K. (d) Shows zoomed in perspective of reflectance in the spectral range (8000–22 500 cm^{-1}) with same legend as (c). The minimum in the high frequency feature redshifts by ≈0.3 eV with increasing temperature.

light source, detector, and reference material used for each spectral range measured in the experiments. Throughout this work we use the scaled frequency ν (cm^{-1}) to represent the spectral range on the x axis of spectroscopy plots [24]. Note that $\nu = f/c$, where f is the frequency of light in Hz, and c is the speed of light in vacuum in cm/s. The frequency label is more appropriate compared to the wave-number label because the frequency remains unchanged whether the light is in vacuum or inside the sample.

LRO single crystals were mounted to a home-built heating stage with Cotronics 950 FS metallic adhesive (2000 °F/ 1366 K max temp). The heating stage was a small brass block (∼1" × 1" × ½") with a central bore and inset clamp to hold the cartridge heater and thermistor respectively. The heating stage was mounted with adjustable standoffs on a piezo stage. The adjustable standoffs are necessary for optical alignment of the sample. The piezo stage allows for translation between our LRO crystals and reference material. The reference material was mounted on a separate stage attached to the piezo stage. The reference material was nominally at room temperature. A heat shield was mounted directly over the heating stage to suppress convective cooling at elevated temperatures. The heat shield also contained an aperture to let through the light beam for the reflectance measurements on the sample. The temperature of the stage was regulated with a Lakeshore 335 temperature controller connected to a Pt 100 Ω thermistor and 300 W Dalton cartridge heater. The heating stage was designed for use up to 600 K and the temperature was maintained within ±1 K at each temperature where data were taken. After crystals were mounted, the top surfaces were cleaved with either scotch tape or mechanically to ensure a fresh surface for the reflectance measurements. Our LRO crystals show different behavior after extended exposure to atmosphere at elevated temperatures. After a temperature dependent measurement, we found that repeating the same measurement on a freshly cleaved surface of the same crystal yielded different results. Therefore, for each spectral range in the infrared and visible, a pristine crystal was mounted, cleaved and measured. Since the direction of the high-symmetry monoclinic b axis is in the plane of the crystal, we considered the possibility of performing polarized reflectance measurements with electric field polarized parallel and perpendicular to the b axis. However, since a pristine crystal was required for each spectral range measured (total of four spectral ranges), it was not feasible to locate the b axis for every crystal. Therefore we used unpolarized incident light for all spectral ranges. These measurements then correspond to the effective in-plane

TABLE I. Experimental details for the different spectral ranges.

	Far Infrared	*Mid Infrared*	*Near Infrared*	*Visible*
Frequency ν Range (cm^{-1})	100–650	650–6000	6000–11 000	11 000–26 000
Light Source	Globar	Globar	Tungsten bulb	Xenon Bulb (75 W)
Detector	Liquid helium cooled bolometer	HgCdTe	InGaAs	Si Photodiode
Spectral Resolution (cm^{-1})	4	4	80	120
Aperture Size (mm)	2.4 × 1.5	1.5 × 0.6	1.2 × 0.6	1.2 × 1.2
Spot Size (μm)	160 × 100	100 × 40	80 × 40	80 × 80
Beam Splitter	Mylar	KBr	CaF_2	CaF_2
Reference Material	Gold	Gold	Gold	Aluminum

reflectance of the surface plane perpendicular to the [101] lattice vector.

After the normalized data (sample spectrum divided by the reference spectrum) were obtained, we multiplied it by the reflectance of gold or aluminum to obtain the absolute reflectance of the LRO sample. The reflectance in each spectral range was then connected to form a continuous spectrum. The systematic uncertainty in the measurement arises from the precision of the optical alignment of the crystal surface relative to the incident light. We estimate this to be a few percent at most, based on comparing multiple optical alignments. The systematic uncertainty is inconsequential because we are mainly interested in changes in the spectra due to temperature variation.

III. RESULTS AND ANALYSIS

Temperature dependent reflectance spectra are presented in Fig. 2(b) on a log scale. Plotted on a linear scale in Figs. 2(c) and 2(d) are the low (250–700 cm^{-1}) and high frequency (8000–22 500 cm^{-1}) absolute reflectance. To model the phonons in the reflectance spectra we used a superposition of Kramers-Kronig consistent Lorentz oscillators. For electronic interband excitations, we employed Tauc-Lorentz oscillators [25] and for electronic, intraband excitations, we use a Drude feature [24]. The fits to the data were performed in the proprietary software WVASE from J. A. Woollam Co. The objective of the fitting process is to obtain the energy-dependent real (ε_1) and imaginary (ε_2) parts of the effective dielectric function. Due to the monoclinic structure of LRO, the optical response is biaxial, and in addition to three distinct diagonal elements, there are nonzero but small off diagonal elements of the complex dielectric tensor [26].Since the crystal has a monoclinic structure, the dielectric tensor cannot be diagonalized, making it difficult to perform a Kramers-Kronig analysis [27] of the reflectance data. The optical conductivity (σ_1) can be directly calculated from the complex dielectric function ε_2. Since the optical conductivity tensor is proportional to the complex dielectric tensor, the optical conductivity tensor will have the same anisotropy as described above for the dielectric tensor. In our measurements with unpolarized incident light, we are probing the optical properties in the plane of the crystal surface that is perpendicular to the [101] lattice vector. Hence, we expect the optical response to be dominated by a mixture of the diagonal elements of the dielectric tensor.

Our model consisted of an LRO layer on top of an epoxy layer. We assumed a frequency independent ε_1 and $\varepsilon_2 = 0$ for the epoxy layer which is consistent with our measured reflectance spectrum of the adhesive. Interference fringes, which indicate backside reflections from the LRO crystal, are present in a limited range in the far- and mid-infrared spectra. The period of these interference oscillations depends on the optical thickness of each crystal. Since different crystals were used for measurements in the far and mid-infrared spectral ranges, these regions were fit simultaneously but with different thicknesses of the LRO crystal layer. The thickness of each crystal was considered a fitting parameter in our reflectance model and was constrained to a range of reasonable thicknesses (25 μm-100 μm). No interference fringes are present in the near-infrared or visible spectra indicating

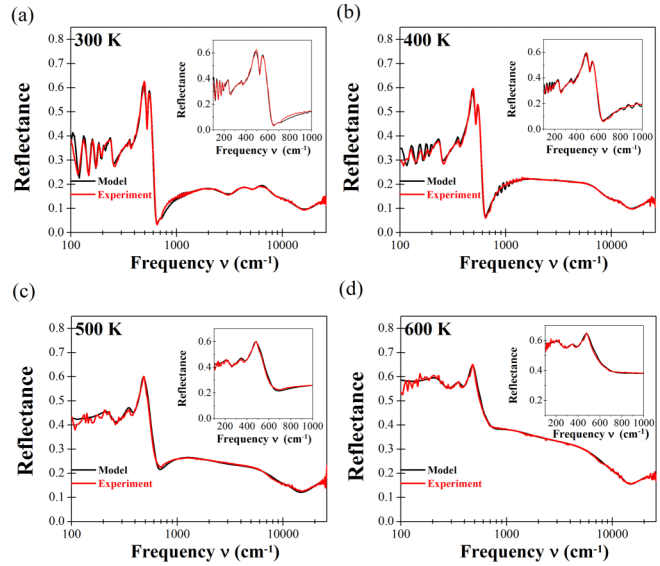

FIG. 3. [(a)–(d)] The measured reflectance data and fits based on the analysis described in the text. Inset shows low frequency ν (100–1000 cm^{-1}) fits of the reflectance.

stronger attenuation of the incident light in the crystals. Simultaneous fits of the absolute reflectance and the interference oscillations in the far and mid-infrared yield accurate values of the real and imaginary parts of the effective dielectric function. Based on the interference fringes in the far- and mid-infrared models, the thicknesses of the crystals used for measurements in these spectral ranges were 48 μm and 36 μm respectively. Since the thicknesses of the two crystals are not too different, the impact on absolute reflectance spectra in the overlapping mid-infrared and far-infrared spectral range can be said to be marginal.

From 300 to 400 K, the mid-infrared interference fringe period is reduced by roughly a factor of ∼2. We suspect that inhomogeneities due to phase coexistence in the vicinity of the phase transition caused the effective refractive index in the mid-infrared to change between 300 and 400 K. In the 500 and 600 K spectra, the far- and mid-infrared interference fringes disappear and the absolute reflectance in these spectral ranges increases thereby indicating a clear increase in the number of free carriers. The experimental reflectance data and reflectance fits based on our model are displayed in Fig. 3. We find quality agreement between our experimental data and the model fits across the entire spectral range. The real ε_1 and imaginary ε_2 parts of the effective dielectric function that describe our reflectance data are displayed in Fig. 4. A large change in the low frequency values of ε_1 and ε_2 between 400 and 600 K, indicates the expected phase transition.

We note that it was necessary to include a minor Drude term to attenuate the amplitude of far-infrared interference fringes in both the 300 and 400 K reflectance spectra, possibly indicating the presence of a small number of free carriers in the VBC phase. We ascribe the weak intraband transitions to free carriers originating from Li vacancies. A previous study found that LRO will dimerize only when it is Li deficient [28]. The existence of these carriers below the critical temperature would also be consistent with previous specific

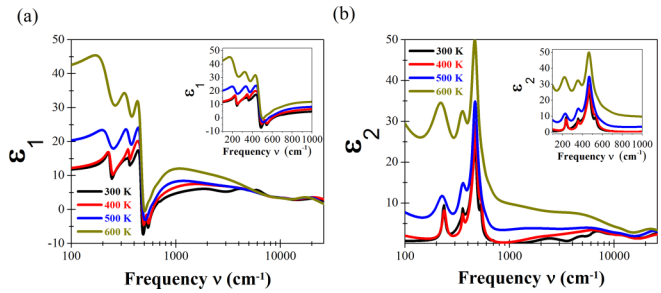

FIG. 4. (a) Real (ε_1) and (b) imaginary (ε_2) parts of the dielectric function obtained from the fits to the reflectance shown in Fig. 3. The inset figures show the dielectric function between 100–1000 cm^{-1}.

heat measurements [16]. Resistivity measurements [10] also show a divergence at low temperature which may be indicative of Kondo screening, further suggesting the presence of free carriers in the VBC phase.

Displayed in Fig. 5(a) is the optical conductivity calculated from the complex dielectric function displayed in Fig. 4(b). The optical conductivity displayed in Fig. 5(a) is predominantly the averaged diagonal elements of the conductivity tensor as discussed earlier. At room temperature and lower energies (<16 000 cm^{-1}), we assign transitions from the weaker (π, δ, δ^*) electrons to (π^*, σ^*) states displayed in Fig. 5(b). We also expect there to be a large, broad contribution to the optical conductivity at higher energies from interband transitions of electrons from the bonding Ru states to antibonding Ru states (σ-σ^*), which is supported by DFT calculations and soft x-ray experiments [14]. These details are presented further in the discussion section.

For comparison with previous dc transport measurements, we extrapolated the optical conductivity [Fig. 5(a)] of our 600 K data down to zero frequency. We obtained a $\sigma_1(\nu \rightarrow 0)$ value of $\approx$30 Ω^{-1} cm^{-1}, which translates to a resistivity value of $\rho(\nu \rightarrow 0) = 0.033$ Ω cm,which is consistent with previous measured values of the dc resistivity [10,16,17]. The high temperature Drude feature has a plasma frequency $\nu_p = \frac{\omega_p}{2\pi c} \approx 210$ cm^{-1} and scattering rate $\gamma = \frac{1}{2\pi c\tau} \approx 111$ cm^{-1}.

IV. DISCUSSION

We first discuss the infrared-active phonons which corresponds to the prominent features at frequencies $\nu <$ 700 cm^{-1}. From group theory analysis the following modes are expected at the Γ point in the low ($P2_1/m$) and high temperatures ($C2/m$) phases respectively [29]

$$\Gamma_{300\ \mathrm{K}} = 20A_g + 16B_g + 20B_u + 16A_u, \quad (1)$$

$$\Gamma_{600\ \mathrm{K}} = 7A_g + 8B_g + 13B_u + 8A_u, \quad (2)$$

where A_g/B_g modes are Raman active and A_u/B_u are infrared active. The width and overlap of phonon modes make individual phonon assignments difficult. The same conclusion was made in a recent study on the Raman vibrational modes of LRO [29]. Strong interference fringes between 100 cm^{-1} and 200 cm^{-1} due to backside reflections from the crystal in the 300 and 400 K spectra are also likely obscuring additional vibrational modes. The prominent double peak feature centered at $\approx$500 cm^{-1} shows a strong dependence on increasing temperature. The vibrational frequencies of these modes suggest they arise from Ru-O bonds. For $T \geqslant 500$ K, the double peak feature is largely gone and instead we observe a single broad phonon peak. Multiple Lorentz oscillators were used to fit the asymmetric profile of this broad peak at 600 K. The Lorentzian form of the complex dielectric function $\tilde{\varepsilon}(\nu)$ used for fits to the phonon features in the reflectance spectra is given by

$$\tilde{\varepsilon}\ (\nu) = \varepsilon_1\ (\nu) + i\varepsilon_2\ (\nu) = \frac{A_n\Gamma_n\nu_o}{\nu_o^2 - \nu^2 - i\Gamma_n\nu} \quad (3)$$

Here A, Γ, and ν_o are the oscillator amplitude, broadening (cm^{-1}) and center frequency (cm^{-1}), respectively. The occurrence of the structural transition from the low temperature, lower symmetry ($P2_1/m$) phase to the higher temperature phase of higher symmetry ($C2/m$) is evident in the reduction of modes. The higher symmetry crystal structure has fewer infrared active phonon modes compared to the lower symmetry crystal structure [29]. Tabulated in Table II are the Lorentz phonon parameters for $T = 300$ and 600 K, respectively. Not

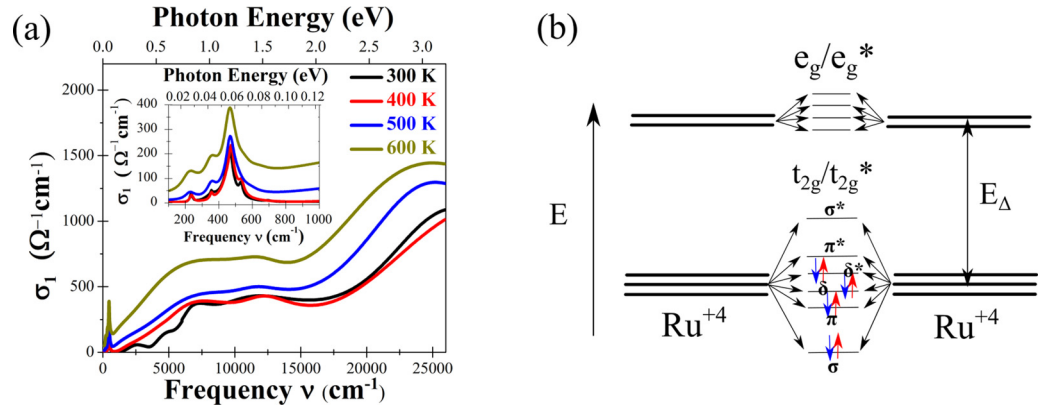

FIG. 5. (a) Real part of the optical conductivity σ_1. Inset shows σ_1 in the frequency range 100–1000 cm^{-1}. (b) Ground state electronic configuration of Ru-Ru dimers below transition temperature. The d orbitals are subject to crystal field splitting which separates states by an energy E_Δ. Due to the large crystal field splitting, the system is in the low spin configuration, filling the lowest states t_{2g}/t_{2g}* (bonding/antibonding) states first. Electrons are shown with up/down arrows.

TABLE II. Lorentz oscillator phonon parameters in the low (300 K) and high (600 K) temperature phases.

300 K ($P2_1/m$)			600 K (C2/m)		
A	Γ	ν_o	A	Γ	ν_o
	(cm^{-1})	(cm^{-1})		(cm^{-1})	(cm^{-1})
0.3	45.0	700.0	1.8	150.0	640.0
5.4	25.8	536.8	3.5	95.4	550.6
20.8	42.4	469.6	36.0	82.0	466.9
7.8	100.0	455.8	14.7	94.8	355.7
4.0	100.0	362.1	18.2	113.2	227.4
2.1	10.0	360.8			

all the allowed infrared-active modes are observed because of the following reasons: weaker modes could be degenerate or have a vanishingly small electric dipole moment; the modes close to each other in frequency may have broad linewidths making it difficult to distinguish between them; and some modes may be screened due to free carriers in the metallic phase.

For the analysis of higher frequency spectra, the formation of molecular orbitals in LRO is highly relevant for describing the dimerization and transport properties [10,14,15,17]. Ru^{4+} has four electrons in its 4*d* shell. These orbitals are fivefold degenerate until they are subjected to an octahedral crystal field. This splits the fivefold degeneracy to two upper states e_g, and three lower t_{2g} states. Due to the large crystal field splitting the electrons arrange in a low spin configuration of the t_{2g} states. σ bonding occurs between the d_{xy} orbitals of neighboring Ru sites [Fig. 6(a)] and is responsible for dimerization. Suitable superposition of the d_{yz} and d_{xz} orbitals results in weakly bound π ($\sim d_{xz} + d_{yz}$) and δ ($\sim d_{xz}$–d_{yz}) bonds as seen in Figs. 6(b) and 6(c). Comparing previously calculated bonding-antibonding splitting energies (t) between these states we see that the σ bond ($t > 2$ eV), is much larger than either π ($t \sim 0.7$ eV) or δ ($t \sim< 0.7$ eV) bonds [15]. The large discrepancy in hopping energies between orbitals, forces the electrons in π or δ bonds to act as largely site centered atomic orbitals [14].

The high frequency peak in the optical conductivity at $\approx$25 000 cm^{-1} or $\approx$3.1 eV at room temperature can be associated with the $\sigma - \sigma^*$ transition, which corresponds to the disassociation of molecular dimers. Establishing this transition, allows us to identify the existence of dimers throughout the measured temperature range. At $T > T_c$, the mean distance between Ru-Ru dimers increases, which reduces the average overlap of the σ bonds, thus reducing the $\sigma \rightarrow \sigma^\star$ transition energy as seen by the red shift in this optical transition in the optical conductivity data [Fig. 5(a)] as well as the reflectance data [Fig. 2(d)]. We would not expect the e_g bands to shift by a significant amount, since their splitting from the t_{2g} band arises from the crystal field splitting E_Δ

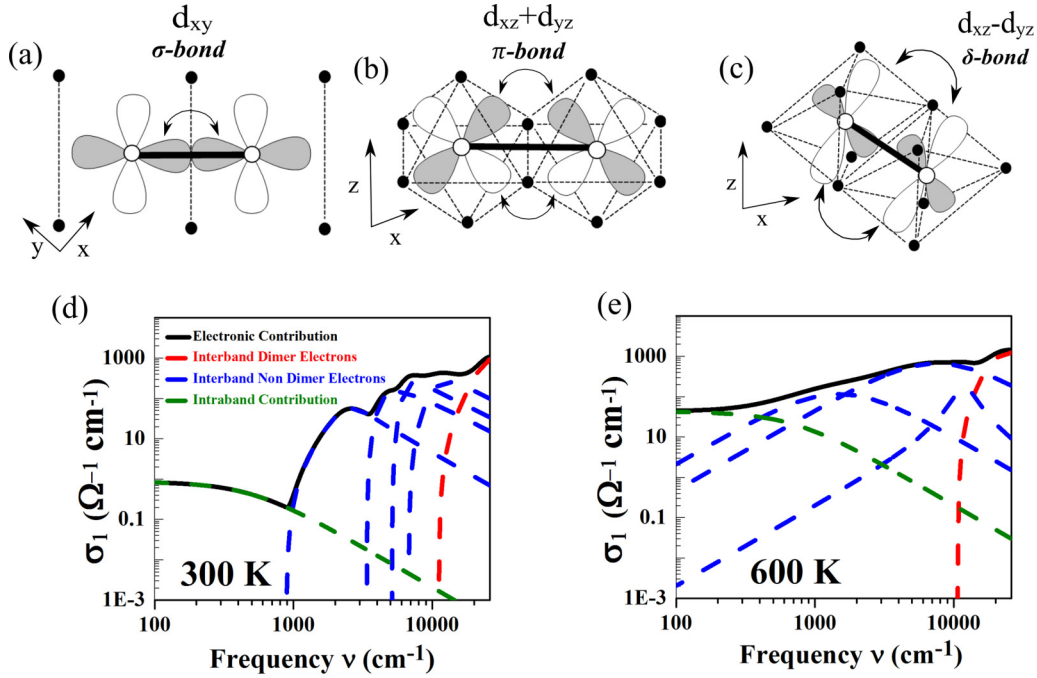

FIG. 6. [(a)–(c)] Molecular bonding picture of Ru dimers. Local coordinates are displayed for each bonding arrangement, where the *x* and *y* axes are directed from Ru to O ions. Open circles represent ruthenium ions, filled circles represent oxygen ligands, and dotted lines are the edges of RuO_6 octahedra. Double sided arrows represent orbital hopping between neighboring sites. Also not presented are all the out of phase antibonding arrangements (σ^*, π^*, δ^*), or hopping pathways to oxygen ligands. (a) The edge sharing nature of the RuO_6 octahedra is such, that the in-plane orbitals (d_{xy}) of neighboring Ru ions have a large overlap, and form σ molecular bonds. [(b) and (c)] Bonds of π and δ symmetry can be constructed by suitable superposition of $d_{xz/yz}$ orbitals. [(d) and (e)] Electronic contribution to optical conductivity σ_1 at $T = 300$ and 600 K respectively. Black lines indicate total electronic contribution, red dashed lines are dimer interband transitions, blue dashed lines are nondimer interband transitions, and green dashed lines are intraband transitions (Drude contribution). Results are plotted log-log to highlight the low frequency electronic contribution to the optical conductivity.

which is governed by the robust RuO_6 octahedra. Therefore we propose that the observed redshift in the $\sigma \rightarrow \sigma^{\star}$ conductivity peak does not arise from optical transitions to the e_g states. It is important to note that we also observe this feature in the electronic structure at $T = 600$ K, indicating the survival of dimers. This is contrary to what we see in the phonon region, where the number of modes has decreased indicating on average the Ru-Ru dimers have vanished. The persistence of dimers for temperatures $\geqslant$500 K despite the structural transition to a higher symmetry phase is explained by temporal fluctuations of the dimers indicating the existence of a VBL phase.

For $T = 300$ K, we can identify an optical band gap with a value of $\approx$110 meV. The presence of a narrow gap is expected and has been shown previously through DFT theory calculations [14,18]. All of the Tauc-Lorentz oscillators in the mid- and near- infrared are gapped below the transition temperature. The gap parameter of these oscillators decreases as the temperature is increased, and for $T \geqslant 500$ K, our data show the optical band gap vanishes. The gap vanishes only for the oscillators in the mid- and near- infrared (electrons in π, δ, and δ^* bonds).

To illustrate the closing of band gaps, plotted in Figs. 6(d) and 6(e) is the electronic contribution (Tauc-Lorentz and Drude components) to the optical conductivity for $T = 300$ and 600 K, respectively. The room temperature contribution has distinct features in the mid- and near-infrared, which are ascribed to transitions from electrons in the π, δ, δ^* bonds to higher energy states. Below an energy $\approx$110 meV, these transitions have zero contribution to the low energy optical conductivity. Whereas the high energy contribution at room temperature is dominated by the $\sigma - \sigma^*$ transition. Above the phase transition, at 600 K, the optical transitions broaden and shift to lower energy. The gaps close for the mid- and near-infrared oscillators. Although their low energy contribution to the optical conductivity is small, with their collective contribution being $\sigma_1(\nu = 100\ \mathrm{cm}^{-1}) \approx 2.8\ \Omega^{-1}\ \mathrm{cm}^{-1}$, as compared to the optical conductivity when including the Drude contribution of $\sigma_1(\nu = 100\ \mathrm{cm}^{-1}) \approx 49\ \Omega^{-1}\mathrm{cm}^{-1}$. The $\sigma - \sigma^*$ transition still has a sizeable bandgap in the high temperature phase ($\approx$1.3 eV), indicating these electrons are still firmly in the molecular orbital picture. For $T \geqslant 500$ K, further evidence of the gap closing can be clearly seen by the large increase in the far-infrared reflectance for frequencies $\nu < 400\ \mathrm{cm}^{-1}$, and disappearance of interference fringes. The large increase in reflectance is also seen in the optical conductivity [Fig. 5(a)], which indicates a large increase in intraband carriers that have to be modeled with a Drude feature. Overall these changes in electronic behavior, signify an insulator-to-metal transition for the electrons in the d_{xz} and d_{yz} orbitals. The closing of the band gap can be explained by the breaking of π and δ bonds, which results in delocalized electrons. Since the electrons from the broken π and δ bonds are not gapped, yet molecular σ bonds still persist locally, the system exhibits orbital selective behavior [21]. It is interesting that the isoelectronic sister compound, Na_2RuO_3, is proposed to be a correlated metal at room temperature [30]. Na_2RuO_3 lacks dimerization, which suggests the importance that Li has on both the structure and transport properties in LRO.

As the temperature is increased, σ_1 across the measured energy range increases for $T \geqslant 500$ K, which represents a large transfer of spectral weight from higher energies to lower energies. This behavior is different from the thermal broadening of the interband transitions observed at 400 K. We suspect that thermally activated σ bond hopping is partially responsible for the increase in spectral weight. A similar dimer hopping model was proposed by Ref. [31] and used to describe transport properties in the intermediate phase of Ti_4O_7 single crystals [32]. In this model, the single electron spectra can be gapped while a continuum of strongly localized two-electron (bipolaronic) and two-hole states exists down to zero energy [31]. As the temperature is increased, thermal activation (0.18 eV or $\approx 1450\ \mathrm{cm}^{-1}$) of these bipolaronic states allows hopping's across a perceived mobility gap to neighboring sites [32]. The hopping represents a transfer of bipolaronic states from high to low energy as the temperature is increased. Since these bipolaronic states exist on the continuum, a broad increase in σ_1 at higher energy is expected. An activation energy has been observed in LRO ($\approx$0.15 eV or $\approx$1200 cm^{-1}) in the high temperature state via dc transport measurements [16,17]. Although this activation energy has been ascribed to a bandgap, we suspect that it represents thermally activated hopping processes. Additionally, O $2p$ orbitals strongly hybridize with the Ru $4d$ states [14,15]. Any energy shift in the Ru $4d$ optical transitions will also therefore occur in optical transitions from the O $2p$ to Ru $4d$ states. Based on this strong hybridization, the observed redshift in the $\sigma \rightarrow \sigma^{\star}$ optical transition through the high temperature phase transition, will also result in a redshift of higher energy O $2p$ to Ru $4d$ optical transition. These red-shifted transitions could then also be partially responsible for the spectral weight increase observed at high temperatures. In general, spectral weight transfers over a large spectral range (of the order of several electron volts) have been observed in other strongly correlated materials [33]. Future ellipsometry measurements on LRO would be needed to quantify this phenomenon.

V. CONCLUSIONS

To conclude, we have obtained temperature dependent, broadband infrared and optical reflectance spectra on single crystals of Li_2RuO_3 (LRO). Through analysis of the reflectance data, we extracted the complex dielectric function and the optical conductivity across the phase transition from a valence bond crystal to a valence bond liquid. From our results we are able to observe the expected structural and electronic phase transition in the vicinity of $T_c \approx 500$ K. The number of phonon modes clearly decreases above the structural transition, indicating a transformation to a more symmetric crystal structure. Even below the expected transition temperature, thermally induced changes to the electronic properties begin to modify our measured reflectance spectra. In the high temperature phase, the optical conductivity spectra support the picture of a valence bond liquid phase originally proposed in Ref. [15]. Additionally, we report direct evidence for orbital-selective metallicity in the high-temperature valence bond

liquid phase. The optical band gap closes for electrons not part of dimerized pairs, while the dimerized electrons are still gapped locally. This valence bond liquid state is therefore a metal-insulator hybrid, with thermally activated dimer hopping coexisting with orbital-selective metallicity.

ACKNOWLEDGMENTS

MMQ acknowledges support from the National Science Foundation (NSF) via Grant No. 1827536. The work at Rutgers University was supported by the DOE under Grant No. DOE: DE-FG02-07ER46382.

[1] K. Ran, J. Wang, W. Wang, Z. Dong, X. Ren, S. Bao, S. Li, Z. Ma, Y. Gan, Y. Zhang, J. T. Park, G. Deng, S. Danilkin, S. Yu, J. Li, and J. Wen, Spin-Wave Excitations Evidencing the Kitaev Interaction in Single Crystalline A - $RuCl_3$, Phys. Rev. Lett. **118**, 107203 (2017).

[2] K. Kitagawa, T. Takayama, Y. Matsumoto, A. Kato, R. Takano, Y. Kishimoto, S. Bette, R. Dinnebier, G. Jackeli, and H. Takagi, A spin–orbital-entangled quantum liquid on a honeycomb lattice, Nature (London) **554**, 341 (2018).

[3] Atsuo Shitade, H. Katsura, J. Kunes, X.-L. Qu, S.-C. Zhang, and N. Nagaosa, Quantum Spin Hall Effect in a Transition Metal Oxide Na_2IrO_3, Phys. Rev. Lett. **102**, 256403 (2009).

[4] A. K. Geim and K. S. Novoselov, The rise of graphene, Nat. Mater. **6**, 183 (2007).

[5] I. I. Mazin, H. O. Jeschke, K. Foyevtsova, R. Valentí, and D. I. Khomskii, Na_2IrO_3 As a Molecular Orbital Crystal, Phys. Rev. Lett. **109**, 197201 (2012).

[6] D. I. Khomskii and S. V. Streltsov, Orbital effects in Solids: basics, recent progress, and opportunities, Chem. Rev. **121**, 2992 (2021).

[7] L. De' Medici, G. Giovannetti, and M. Capone, Selective Mott Physics As a Key to Iron Superconductors, Phys. Rev. Lett. **112**, 177001 (2014).

[8] A. Kostin, P. O. Sprau, A. Kreisel, Y. X. Chong, A. E. Böhmer, P. C. Canfield, P. J. Hirschfeld, B. M. Andersen, and J. C. S. Davis, Imaging orbital-selective quasiparticles in the hund's metal state of fese, Nat. Mater. **17**, 869 (2018).

[9] Y. Shimizu, H. Takeda, M. Tanaka, M. Itoh, S. Niitaka, and H. Takagi, An orbital-selective spin liquid in a frustrated heavy fermion spinel LiV_2O_4, Nat. Commun. **3**, 981 (2012).

[10] Y. Miura, Y. Yasui, M. Sato, N. Igawa, and K. Kakurai, New type phase transition of Li_2RuO_3 with honeycomb structure, J. Phys. Soc. Jpn. **76**, 033705 (2007).

[11] V. Hermann, M. Altmeyer, F. Freund, A. Jesche, A. A. Tsirlin, M. Hanfland, P. Gegenwart, I. I. Mazin, D. I. Khomskii, R. Valentí, and C. A. Kuntscher, Competition between spin-orbit coupling, magnetism, and dimerization in the honeycomb Iridates: α -Li_2 IrO_3 under pressure, Phys. Rev. B **97**, 020104(R) (2018).

[12] L. S. I. Veiga, K. Glazyrin, G. Fabbris, C. D. Dashwood, J. G. Vale, H. Park, M. Etter, T. Irifune, S. Pascarelli, D. F. Mcmorrow, T. Takayama, H. Takagi, and D. Haskel, Pressure-Induced structural dimerization in the hyperhoneycomb iridate β -Li_2 IrO_3 at low temperatures, Phys. Rev. B **100**, 064104 (2019).

[13] G. Bastien, G. Garbarino, R. Yadav, R. B. Rodríguez, Q. Stahl, M. Kusch, S. P. Limandri, R. Ray, D. G. Mandrus, S. E. Nagler, M. Roslova, A. Isaeva, and T. Doert, Pressure-Induced dimerization and valence bond crystal formation in the kitaev-heisenberg magnet α-$RuCl_3$, Phys. Rev. B **97**, 241108(R) (2018).

[14] Z. V. Pchelkina, A. L. Pitman, A. Moewes, E. Z. Kurmaev, T. Tan, D. C. Peets, J. Park, and S. V. Streltsov, Electronic structure of Li_2 RuO_3 studied by LDA and LDA+DMFT calculations and soft x-Ray spectroscopy, Phys. Rev. B **91**, 115138 (2015).

[15] S. A. J. Kimber, I. I. Mazin, J. Shen, H. O. Jeschke, S. V. Streltsov, D. N. Argyriou, R. Valenti, and D. I. Khomskii, Valence bond liquid phase in the honeycomb lattice material Li_2RuO_3, Phys. Rev. B **89**, 081408(R) (2014).

[16] J. Park, T. Tan, D. T. Adroja, S. Choi, D. Cho, S. Lee, J. Kim, H. Sim, T. Morioka, and H. Nojiri, Robust singlet dimers with fragile ordering in two-dimensional honeycomb lattice of Li_2RuO_3, Sci. Rep. **6**, 25238 (2016).

[17] S. Yun, K. H. Lee, S. Y. Park, T. Tan, J. Park, S. Kang, D. I. Khomskii, Y. Jo, and J. Park, Magnetic and electrical anisotropy with correlation and orbital effects in dimerized honeycomb ruthenate Li_2RuO_3, Phys. Rev. B **100**, 165119 (2019).

[18] Y. Miura, M. Sato, Y. Yamakawa, T. Habaguchi, and Ō. Yoshiaki, Structural transition of Li_2RuO_3 induced by molecular-orbit formation, J. Phys. Soc. Jpn. **78**, 094706 (2009).

[19] S. A. J. Kimber, C. D. Ling, D. J. P. Morris, A. Chemseddine, P. F. Henry, and D. N. Argyriou, Interlayer tuning of electronic and magnetic properties in honeycomb ordered Ag_3LiRu_2O, J. Mater. Chem. **20**, 8021 (2010).

[20] A. L. Buzlukov, I. Yu. Arapova, A. Y. . Germov, T.-Y. Tan, K.N.Mikhalev, J.-G. Park, and S. V. Streltsov, Magnetic properties of Li_2 RuO_3 as studied by NMR and LDA+ DMFT calculations, JETP Lett. **105**, 375 (2017).

[21] S. V. Streltsov and D. I. Khomskii, Orbital-Dependent singlet dimers and orbital-selective peierls transitions in transition-metal compounds, Phys. Rev. B **89**, 161112(R) (2014).

[22] J. C. Wange, T. F. Qi, J. Terzic, S. J. Yuan, F. Ye, S. V. Streltsov S. Aswartham, R. K. Kaul, D. I. Khomskii, and G. Cao, Lattice-Tuned magnetism of $Ru4 + (4d^4)$ ions in single crystals of the layered honeycomb ruthenates Li_2RuO_3 and Na_2RuO_3, Phys. Rev. B **90**, 161110(R) (2014).

[23] K. Momma and F. Izumi, Vesta 3 for three-dimensional visualization of crystal,volumetric and morphology data, J. Appl. Crystallogr. **44**, 1272 (2011).

[24] M. Dressel and G. Gruner, *Electrodynamics of Solids: Optical Properties of Electrons in Matter*, 1st ed. (Cambridge University Press, Cambridge, UK, 2002).

[25] G. E. Jellison and F. A. Modine, Parameterization of the optical functions of amorphous materials in the interband region, Appl. Phys. Lett. **69**, 371 (1996).

[26] Y. Petit, S. Joly, P. Segonds, and B. Boulanger, Recent advances in monoclinic crystal optics, Laser Photon. Rev. **7**, 920 (2013).

[27] M. Dressel, B. Gompf, D. Faltermeier, A. K. Tripathi, J. Pflaum, and M. Schubert, Kramers-Kronig-Consistent optical functions

of anisotropic Crystals: Generalized spectroscopic ellipsometry on pentacene, Opt. Express **16**, 19770 (2008).

[28] K. Hoang, M. Oh, and Y. Choi, Electronic structure and properties of lithium-rich complex oxides, ACS Appl. Electron. Mater. **1**, 75 (2019).

[29] Y. S. Ponosov, E. V. Komleva, and S. V. Streltsov, Phonon anomalies near the magnetostructural transition in Li_2RuO_3: Raman spectroscopy and density functional theory studies, Phys. Rev. B **100**, 134310 (2019).

[30] L. S. I. Veiga, M. Etter, E. Cappelli, H. Jacobsen, J. G. Vale, C. D. Dashwood, D. Le, F. Baumberger, D. F. McMorrow, and R. S. Perry, Correlated electron metal properties of the honeycomb ruthenate Na_2RuO_3, Phys. Rev. Materials **4**, 094202 (2020).

[31] P. W. Anderson, Model for the Electronic Structure of Amorphous Semiconductors, Phys. Rev. Lett. **34**, 953 (1975).

[32] S. Lakkis, B. K. Chakraverty, C. Schlenker, R. Buder, and M. Marezio, Metal-Insulator transitions in Ti_4O_7 single Crystals: crystal Characterization, specific Heat, and electron paramagnetic resonance, Phys. Rev. B **14**, 1429 (1976).

[33] M. M. Qazilbash, A. A. Schafgans, K. S. Burch, S. J. Yun, B. G. Chae, B. J. Kim, H. T. Kim, and D. N. Basov, Electrodynamics of the vanadium oxides VO_2 and V_2O_3, Phys. Rev. B **77**, 115121 (2008).